

Microstructural Transformation of Cold-Sprayed GRCop-42 for Rocket Engine Combustion Chamber Liners

A Senior Project

Presented to

The Faculty of Materials Engineering

California Polytechnic State University, San Luis Obispo

In Partial Fulfillment

Of the Requirements for the Degree

Bachelor of Science

By

Mason Souther

© 2019 Mason Souther

Abstract

Rocket engines have always relied on high-conductivity copper liners to protect structural components from extreme thermal loads produced by combustion. Forged NARloy-Z has been the material of choice for decades but increasing cost of its constituent silver and high waste in the machining process has reduced the alloy's cost effectiveness. Aerojet Rocketdyne wants to determine the viability of cold-spray additively manufactured GRCo-42 as a replacement alloy to reduce liner cost. Screening tests were performed to observe the microstructural development and microhardness changes of cold-sprayed GRCo-42 after being subjected to multiple stages of the typical heat treatment of a combustion chamber liner. Two batches of samples with different cold-spray parameters were given one of four treatments: as-sprayed, HIPed, HIPed and annealed at 1700°F, and HIPed and annealed at 1800°F. Statistical analysis of hardness data concluded a reduction in mean hardness from 197HV to 119HV after HIPing and an additional reduction to 86HV after the annealing treatment. The temperature of the annealing was statistically insignificant. Optical microscopy revealed 'healing' of former powder boundaries after annealing treatment, indicated by the boundaries no longer being preferentially etched. These heat treatment effects suggest an increase in yield strength and low-cycle fatigue life, with fewer crack propagating, high-energy boundaries present. No reliable data could be collected on particle coarsening due to natural particle size variance.

Keywords

Copper alloy, GRCo-42, cold spray additive manufacturing, high temperature material, microhardness, annealing, particle coarsening, optical microscopy, metallography, combustion chamber liners, rocket engines, materials engineering

Acknowledgements

Thank you to each of those listed for their contributions. Without your support this project would not have been possible.

Aerojet Rocketdyne: sponsoring this research project.

Bryce Simmons: supporting the development and progression of the project.

Prof. Blair London: advising me through the project and being a driving force toward sample procurement.

David Webster: running the SEM for examination of sample surfaces.

Hajime Yamanaka: extensive consultation for statistical analysis.

Maddie Reed: running EDS for examination of oxides.

Contents

1.	Introduction	1
1.1	Stakeholders.....	1
1.2	Broader Impacts.....	1
1.3	Background.....	1
1.3.1	Aerojet Rocketdyne	1
1.3.2	Main Combustion Chamber Liners	3
1.3.3	Cold Spray Additive Manufacturing	5
1.3.4	Copper Alloys and GRCop-42	8
1.4	Problem Statement.....	13
2.	Experimental Procedure.....	14
2.1	Heat Treatments and Sample Preparation.....	14
2.2	Microhardness Testing.....	15
2.3	Optical and Scanning Electron Microscopy	15
2.4	Safety.....	16
3.	Results	16
3.1	Optical Microscopy	16
3.1.1	Etched Surfaces	16
3.1.2	Powder Microscopy.....	18
3.2	Microhardness Data	18
3.3	Scanning Electron Micrographs.....	19
3.3.1	Surface Analysis	19
3.3.2	Oxide Analysis	21
3.4	Particle Size Distributions	23
4.	Discussion.....	24
4.1	Optical Microscopy	24
4.1.1	Possible Effect on Fracture Toughness and LCF life	24
4.1.2	Possible Effect on Thermal Conductivity.....	25
4.2	Microhardness	25
4.3	SEM.....	27
4.4	Particle Size Distributions	28
5.	Conclusions	30
6.	Recommendations	31
7.	References	31
8.	Appendix	32
8.1	Heat Treatment Certifications	32

List of Figures

Figure 1: Image of the F-1 rocket engine, capable of producing 1.5 million pound-force of thrust and standing 18.5 feet tall ¹	2
Figure 2: Model of Aerojet Rocketdyne’s newest rocket engine design, AR1, promising to be all American made, low cost, and be compatible with multiple launch vehicles ²	2
Figure 3: Schematic of the basic inner workings of a liquid rocket engine, where fuel and an oxidizer react within a combustion chamber to produce heat and thrust ³	3
Figure 4: Main combustion chamber manufactured from GRCop-84 using vacuum plasma spraying. The converging-diverging conical shape allows for an increase of thrust and is typical of rocket engine exhaust geometry ⁴	4
Figure 5: Cross sectional examination of one method of cooling an MCC liner, with grooves cut out acting as coolant channels. ⁵	4
Figure 6: Example of cold spray in application for coating(a), repair(b) and additive manufacturing(c) ⁸	6
Figure 7: Schematic of the cold spray process, where powder is accelerated with heated gas through a deLaval nozzle, where the velocity is increased significantly with decrease in nozzle diameter ⁹ . Note that the heated gas does not significantly heat the powder to the extent that it will melt.....	6
Figure 8: Stress-strain responses of copper after various annealing treatments post-cold spray compared to bulk copper. The as-sprayed coating displays ceramic-like behavior, failing at significantly reduced levels of strain ¹²	7
Figure 9: Stages of heat treatment’s effect on a cold sprayed microstructure with varying porosity. Both cases show the effect of treatment on the powder morphology, with individual powder particle boundaries being dissolved as recrystallization and grain growth occurs ¹²	8
Figure 10: SEM image of GRCop-84 powder, a copper matrix containing 14 volume percent Cr ₂ Nb particles ⁴	9
Figure 11: 0.2% offset yield strength of various aerospace copper alloys. As-consolidated and brazed GRCop-84 has a high retention rate of yield strength compared to competitors due to its strengthening phase being incredibly temperature stable ¹⁴	10
Figure 12: Plot of the comparison of thermal conductivity of various engineering copper alloys, highlighting the benefit of GRCop-42 over mechanically-superior GRCop-84 ⁶	11
Figure 13: Comparison of the low-cycle-fatigue life of the GRCop alloys to NARloy-Z. Despite significantly higher thermal conductivity and nearly identical strengths, GRCop-42 has a nearly identical LCF life to NARloy-Z, only slightly reduced from GRCop-84 ⁶	12
Figure 14: Effect of annealing treatments at a range of temperatures on cold-sprayed GRCop-42 microhardness. With low porosity, these trends will be roughly correlated to the effect on tensile strength and inversely so ductility ¹³	12
Figure 15: As-sprayed samples of cold-sprayed GRCop-42 (a) 2B and (b) 3C. Each designation denotes a different set of confidential cold-spray parameters.	14
Figure 16: Diagram of sample geometry referencing the build direction.	15
Figure 17: Etched micrographs of sample (a) 2B and (b) 3C in the as-sprayed condition reveal preferentially etched grain boundaries and clearly visible Cr ₂ Nb particles.....	17
Figure 18: Etched micrographs of sample (a) 2B and (b) 3C in the HIPed condition have reduced darkening of grain boundaries compared to the as-sprayed samples.	17
Figure 19: Etched micrographs of sample (a) 2B and (b) 3C after a 1700°F anneal no longer show significant contrast at grain boundaries, instead having a more uniform etch.....	17
Figure 20: Etched micrographs of sample (a) 2B and (b) 3C after a 1800°F anneal show the same uniform etch as seen in the 1700°F anneal.	17
Figure 21: Compilation of 1000x magnification micrographs of powder particles. Cr ₂ Nb particles within are clearly visible in the unetched condition.	18
Figure 22: Plot of microhardness vs treatment for each cold-sprayed sample, showing a relationship between increased heat treatment duration and reduced microhardness. Statistical analysis is needed to determine the significance of any differences.	19
Figure 23: The etched surface of sample 2B-AS with grain boundaries being etched preferentially. Signs of porosity and increased deformation in some areas are also present.....	20

Figure 24: Etched surface of sample 3C-HIP reveals grain boundaries and Cr ₂ Nb particles that lie within and between them.	20
Figure 25: Etched surface of sample 3C-18 reveals some etching of grain boundaries, but primarily the etching of the surface.	21
Figure 26: SEM image depicting multiple oxides on the surface of sample 2B-AS.	21
Figure 27: SEM image and composition of an oxide present on the surface of sample 2B-AS, with results not containing any unexpected elements and likely being a copper-based oxide.	22
Figure 28: SEM image of a dark oxide from sample 2B-AS shows a visual difference from the oxide in Figure 23, but compositionally the two are likely identical.	22
Figure 29: EDS analysis of two adjacent oxides reveals similar compositions that are different than those sampled in Figure 23 and Figure 24.	22
Figure 30: Particle size distributions for sample (a) 2B and (b) 3C shows a non-normal distribution, instead being right skewed. The shape of the distributions indicates that ANOVA cannot be used.	23
Figure 31: Plot of the median particle diameter for each sample across all treatment levels. High error due to manual measurement likely influenced the high standard deviation.	24
Figure 32: (a) Microhardness value clearly follows a normal distribution, with no significant non-linearity of the residuals. (b) Versus fits shows the even distribution around a residual of 0, indicating that there were no effects that would require a transformation of the data to meet ANOVA requirements. (c) Is a visual representation of the normal distribution and (d) versus order shows the randomness of the data with no evident skews.	26
Figure 33: Analysis of the effect of each factor, being ID or Process, shows that sample 3C is statistically significantly harder than sample 2B. Comparing the different processing methods, as-sprayed is the hardest and is different than HIP, and HIP is harder and different than -17 and -18. There is no significant microhardness difference between the -17 and -18 treatments.	27
Figure 34: Sample 2B-AS at 1000x magnification shows the natural variance of Cr ₂ Nb particles within the as-sprayed structure. Hand-counting particles can result in widely different size distributions depending on the area sampled.	30

List of Tables

Table I: Summary of Sample Designations and Their Treatments	14
Table II: Indentation Size and Resulting Microhardness Data for Sample 2B	18
Table III: Indentation Dimensions and Resulting Microhardness Data for Sample 3C	19
Table IV: Mean, Median, and Standard Deviation of Particle Diameters in Sample Groups 2B and 3C	23
Table V: ANOVA Test Results Determining the Significance of Each Factor	26
Table VI: MiniTAB Output for Sample 2B Non-Parametric Comparison	28
Table VII: MiniTAB Output for Sample 3C Non-Parametric Comparison	29

1. Introduction

1.1 Stakeholders

The primary stakeholders involved with this project are Aerojet Rocketdyne, the company responsible for the collection and integrity of the data reported on in this paper as well as NASA, who commissioned the work to Aerojet Rocketdyne. Improving the production of critical components such as the main combustion chamber liner is always a benefit to the company's manufacturing and assembling of systems as complex as rocket engines, and the determination of manufacturing viability can open the door to less expensive and easier production of more components later.

1.2 Broader Impacts

The significance of this research is potentially large depending on the level of commitment manufacturers are willing to make into cold spray additive manufacturing. The ability to manufacture hollow components from materials in the powder state is an important step into increasing the speed and price in which large components could be produced. If cold spray can replace forging and casting manufacturing for large components that are not mass produced without property trade-offs, manufacturing of aerospace and high-performance components in general could change significantly in the next decade.

1.3 Background

1.3.1 Aerojet Rocketdyne

Aerojet Rocketdyne is a developer and manufacturer of rocket propulsion systems in the defense industry. Having developed the F-1 engine ([Figure 1](#)) for the Saturn V launch vehicle, the RS10 engine on the more recent Delta IV launch vehicle, and various others, Aerojet Rocketdyne has a long and successful history of producing rocket engines.



Figure 1: Image of the F-1 rocket engine, capable of producing 1.5 million pound-force of thrust and standing 18.5 feet tall¹.

The significant amount of thrust needed to transport a rocket's payload into space produces a significant amount of heat as a byproduct. Supporting extreme thermal loads requires cooling of the combustion chamber to prevent the degradation of the mechanical properties of supporting structures. These cooling systems necessitated the development of temperature resistant, high thermal conductivity copper alloys including NARloy-Z, the alloy used for the cooling systems of the F-1 rocket engine. As Aerojet Rocketdyne continues development of their new AR1 rocket engine (**Figure 2**), new and advanced copper alloys and manufacturing methods are being developed and applied. Aerojet Rocketdyne is currently investing heavily into selective laser melting (SLM), a metallic additive manufacturing technique. Collaboration with NASA has also allowed for the studying of copper alloys to replace NARloy-Z as a main combustion chamber liner material.



Figure 2: Model of Aerojet Rocketdyne's newest rocket engine design, AR1, promising to be all American made, low cost, and be compatible with multiple launch vehicles².

1.3.2 Main Combustion Chamber Liners

While the full explanation of the workings of liquid rocket engine mechanics (LREs) falls outside the scope of this research project, knowledge of the systems operations is helpful to understand the significance of this project. LREs function by pumping high pressure liquid fuel and an oxidizer into a main combustion chamber (MCC). Through thermal and chemical reactions, the resulting blend combusts and outputs significant pressure and heat, the former of which is utilized as thrust (Figure 3).

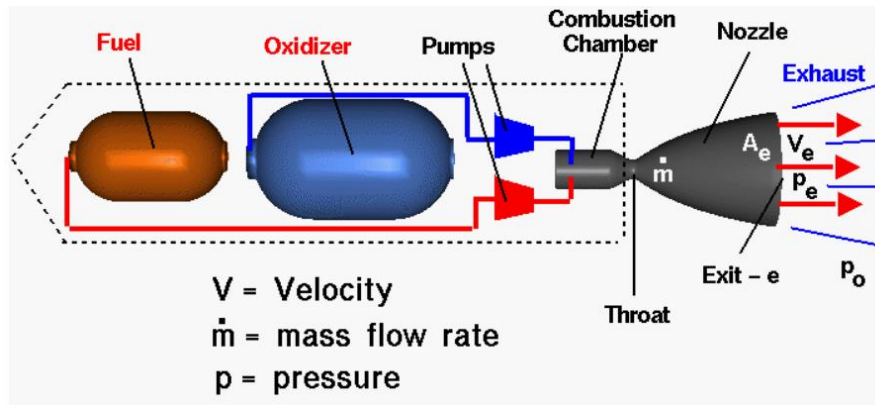


Figure 3: Schematic of the basic inner workings of a liquid rocket engine, where fuel and an oxidizer react within a combustion chamber to produce heat and thrust³.

Increasing payload mass requires more thrust and fuel to leave Earth's atmosphere. While increasing thrust is desirable, the counterbalance is the increasing thermal load applied to the combustion chamber and exhaust nozzle; it does not matter how much thrust your engine can produce if it cannot support the applied thermal load without compromising structural integrity of supporting structures. Production of large rocket engines such as Aerojet Rocketdyne's F-1, which produced over 1.5 million force-pounds of thrust¹ required advanced cooling systems to prevent failure. The cooling system of rocket engine combustion chambers is centered around the main combustion chamber liner (Figure 4), a thermally conductive skin that lines the inside of the MCC and the exhaust in the shape of a DeLaval nozzle.



Figure 4: Main combustion chamber manufactured from GRCop-84 using vacuum plasma spraying. The converging-diverging conical shape allows for an increase of thrust and is typical of rocket engine exhaust geometry⁴.

The MCC liner acts as a heat sink, transmitting thermal energy from the combustion chamber to a cooling agent that is pumped through channels surrounding or machined into the liner, removing heat from the combustion chamber (**Figure 5**). The cooling agent is either recirculated and cooled for re-use or jettisoned at the end of the liner into open air.

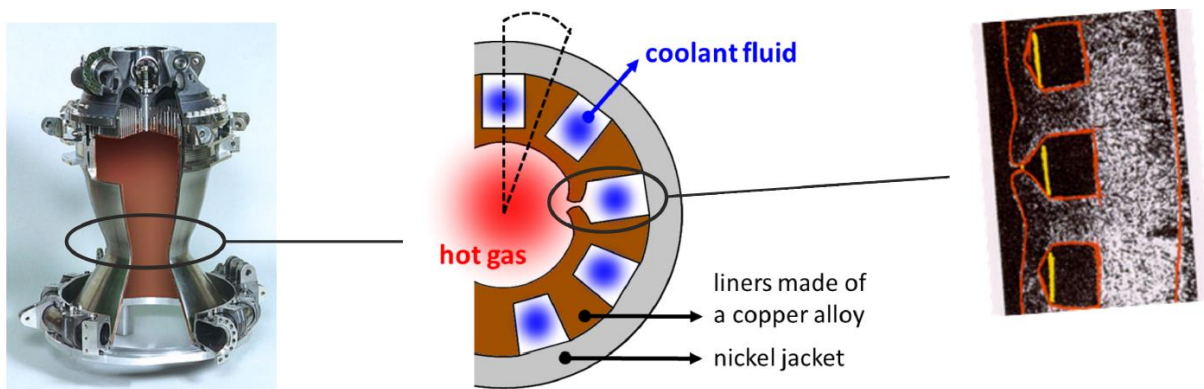


Figure 5: Cross sectional examination of one method of cooling an MCC liner, with grooves cut out acting as coolant channels.⁵

The defining property of MCC liners is thermal conductivity; higher conductivity allows for more efficient transferring of heat from the combustion chamber to the cooling agent. Thermal conductivity is not an ‘end all be all’ of properties though. The high operating temperatures of combustion chambers require alloys engineered to retain mechanical properties at highly elevated temperatures, qualifying

copper alloys such as NARloy-Z and the GRCop family. Each of these copper alloys has a relatively high thermal conductivity, the presence of grain-boundary-pinning particles, and a resistance to oxidation and hydrogen embrittlement, all required for proper liner functionality. The cyclic nature of heating cycles also leads to vulnerabilities to fatigue-driven failure and is the primary failure mode of MCC liners.

While there are currently established methods of producing rocket engine components to meet current requirements, further improvements of resulting properties, cost, and manufacturing ease are always in development for new generations of rocket engine components, combustion chamber liners included. The total engine assembly can take three to four years to complete, requiring the collaboration of multiple manufacturing companies⁷. Manufacturing these components with the highest degree of quality to meet the required properties is critical, and development of new and advanced manufacturing techniques to ease this process are highly sought after. Current MCC liners have multiple manufacturing options; one of which involves the casting of a copper alloy into shape before being machined and hot-roll-contoured into its final hourglass shape⁷. Streamlining the manufacturing process of this component would reduce cost and waste significantly in addition to the removal of multiple operations. One advanced technique that is finding increased popularity is additive manufacturing (AM), more commonly known as 3D-printing, being able to manufacture complex components with little wasted material. There are multiple types of AM for metals, with various starting material requirements, joining mechanisms, and resulting component properties. One of these types that will be explored in this project is cold spray additive manufacturing.

1.3.3 Cold Spray Additive Manufacturing

Cold spray additive manufacturing (CSAM) is a powder-based solid-state manufacturing process initially designed for the application of metallic coatings. Contrasted to many other additive manufacturing methods such as selective laser melting (SLM), cold spray does not involve a heating process, instead relying on kinetic energy for powder bond formation. By accelerating small (typically 10-50 μ m in diameter) particles of the desired metal powder at a substrate, low porosity, resilient metallic coatings can be applied to solid surfaces without causing thermal damage. Advancement of the cold spray coating process led to development of additive manufacturing of full components and component repair with this powder-accelerant based method ([Figure 6](#)).



Figure 6: Example of cold spray in application for coating(a), repair(b) and additive manufacturing(c)⁸.

As previously mentioned, CSAM is done through the rapid acceleration of metallic powders toward a solid substrate, whether a component to be repaired, a substrate requiring coating, or a build platform. To form a tough and resilient layer of material the powder must be given enough kinetic energy such that impact with the substrate will cause the powder to undergo massive plastic deformation and adiabatic heating to bond with its neighbors⁹. Typical velocities of powders as they impact the solid substrate exceed 300m/s⁸ and are achieved by pressurizing a gas through a DeLaval nozzle as an acceleration mechanism (Figure 7). Studying of the ideal powder velocities, impact angles, and mechanics of the deformation has been performed extensively; the last of which was done through finite element analysis alongside comparisons to experimental values by Assadi⁹, Meng¹⁰, Gilmore¹¹, and others but falls outside the scope of this research.

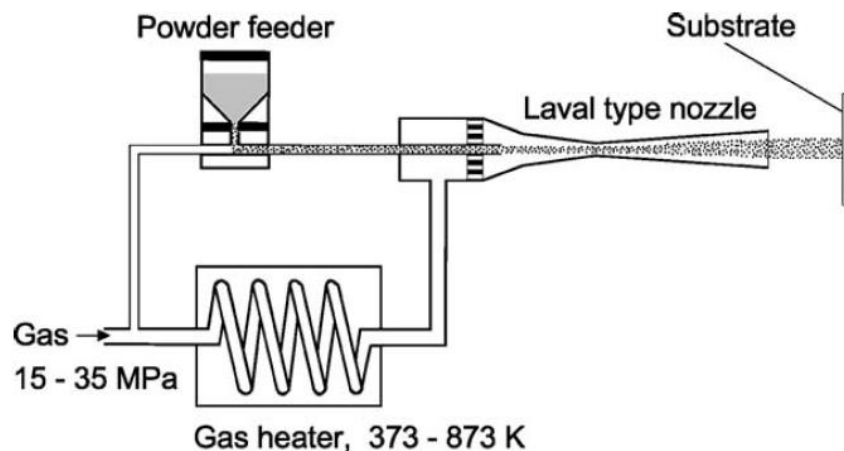


Figure 7: Schematic of the cold spray process, where powder is accelerated with heated gas through a deLaval nozzle, where the velocity is increased significantly with decrease in nozzle diameter⁹. Note that the heated gas does not significantly heat the powder to the extent that it will melt.

Achieving the proper ‘splating’ mechanics of massive plastic deformation and adiabatic heating of powder particles requires speeds above some ‘critical velocity’, ensuring the powder particle has enough kinetic energy. The critical velocity for ideal resulting properties of a powder is a function of material hardness, density, and powder diameter¹¹. A metal with a higher specific strength (ratio of strength to density) such as titanium requires more kinetic energy, and thus higher speeds, to ‘splat’ properly. Conversely, more ductile and dense materials such as copper have lower critical velocities and typically form less porous structures¹². The deformation and adiabatic-heating based bonding mechanism has multiple benefits and drawbacks. The lack of a liquid-to-solid phase transformation allows for retention of microstructural features such as particles while preventing the growth of any undesirable phases or particles during the cooling process. Additionally, cold sprayed components typically have lower porosity than those additively manufactured with liquid-state techniques, improving their mechanical properties and reducing the necessity of hot isostatic pressing (HIPing) as an additional processing step¹³. However, the lack of a significant thermal input and presence of significant plastic deformation makes the material properties of an as-sprayed component nearly ceramic in nature, with as-sprayed ductility typically less than 0.5%, even for metals as ductile in a bulk state as copper¹² (Figure 8).

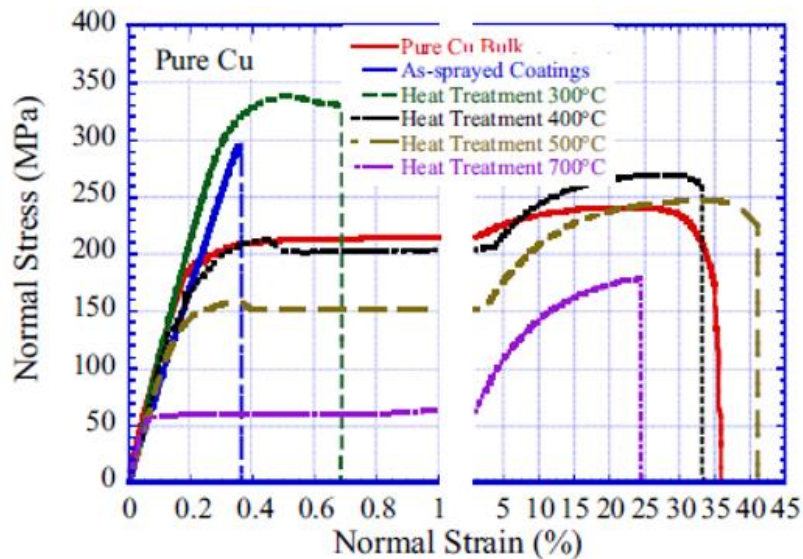


Figure 8: Stress-strain responses of copper after various annealing treatments post-cold spray compared to bulk copper. The as-sprayed coating displays ceramic-like behavior, failing at significantly reduced levels of strain¹².

This brittleness is unacceptable for most applications, so the components are rarely usable in the as-sprayed condition. To solve this, heat treatments (typically annealing) are done prior to component use or further processing. In addition to the stress-relief brought on by the annealing of the deformed grains, heat treatments act as an additional binding mechanism between ‘splatted’ powder particles. This process has four main stages (Figure 9), with the additional binding mechanism occurring as grains grow between

regions previously occupied by separate particles of powder through diffusion and recrystallization. The effect of heat treatment on the mechanical properties is significant, as is evident from **Figure 8**, ductility being increased significantly between as-sprayed and high-temperature annealed copper. Studying the effect of heat treatments on various cold-spray compatible alloys is necessary for the application of CSAM in critical components. The minimal waste and lack of a thermal input make cold spray a valuable technique for manufacturing.

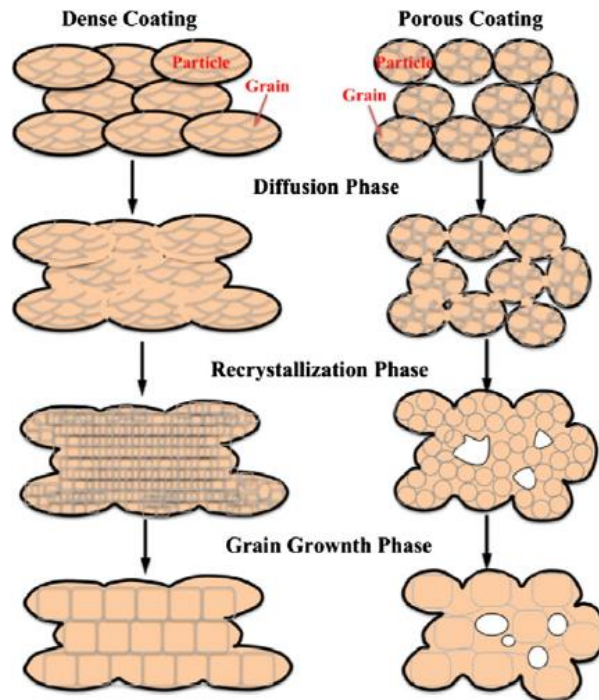


Figure 9: Stages of heat treatment's effect on a cold sprayed microstructure with varying porosity. Both cases show the effect of treatment on the powder morphology, with individual powder particle boundaries being dissolved as recrystallization and grain growth occurs¹²

1.3.4 Copper Alloys and GRCop-42

As mentioned previously, the requirements for an MCC liner are high thermal conductivity, low-cycle-fatigue resistance, a high temperature strengthening mechanism, and a resistance to oxidation and hydrogen embrittlement. The high thermal conductivity requirement for MCC liners qualify copper alloys as constituent materials, with thermal conductivities for most engineering copper alloys exceeding $260 \text{ W/m} \cdot \text{K}$ compared to about $180 \text{ W/m} \cdot \text{K}$ for aluminum and $20 \text{ W/m} \cdot \text{K}$ for stainless steels. To maximize thermal conductivity within this select class of materials, knowledge of strengthening mechanisms and their impact on thermal conductivity is needed. When alloying copper, thermal conductivity will always be reduced in a trade-off for mechanical properties. Say, for instance, one decides to strengthen an alloy by introducing a second phase as individual grains. While the mechanical properties would likely be improved by impeding dislocation motion, introducing high amounts of

secondary phases into highly conductive copper alloys reduces their thermal conductivity significantly as electron mobility is also reduced by a potentially less-conductive second phase. Through proper types of strengthening, these reductions can be minimized while adding significant strength. Solid solution strengthening is a poor alloying method for high conductivity copper as it reduces the conductivity of every region of the material. Conversely, precipitation hardened alloys limit conductivity reductions through the segregation of alloying elements to their strengthening particles, producing conductivity ‘highways’ around the less-conductive particles. A similar concept is seen with the high conductivity copper alloys such as ETP copper used for conducting electricity: rather than have impurities dissolved in solution, the copper is alloyed with a small amount of oxygen to group the impurities into oxides. While these compounds have reduced conductivity, they are only present in a fraction of the overall volume, minimizing their reduction of conductivity. Increasing the volume fraction of particles may increase mechanical properties, but it does so at the cost of reduced conductivity, so careful consideration of the balance of mechanical and thermal properties is needed.

The alloy of interest for this project is GRCop-42, a copper alloy developed at NASA’s Glenn Research base in Cleveland, Ohio. Composed of 4at% chromium, 2at% niobium, and the balance copper, GRCop-42 is a member of the Cu-Cr-Nb family of copper alloys alongside GRCop-84 which has twice the atomic percent of either alloying element. Both GRCop-84 and GRCop-42 are powder alloys, having to be produced by powder atomization⁴. The reason for this lies with the strengthening mechanisms of the alloy: primarily grain size, but with Cr_2Nb particles acting as grain boundary pinners and strengtheners. These particles compose ideally 14% of the GRCop-84 microstructure (Figure 10) and by extension 7% of the GRCop-42 microstructure.

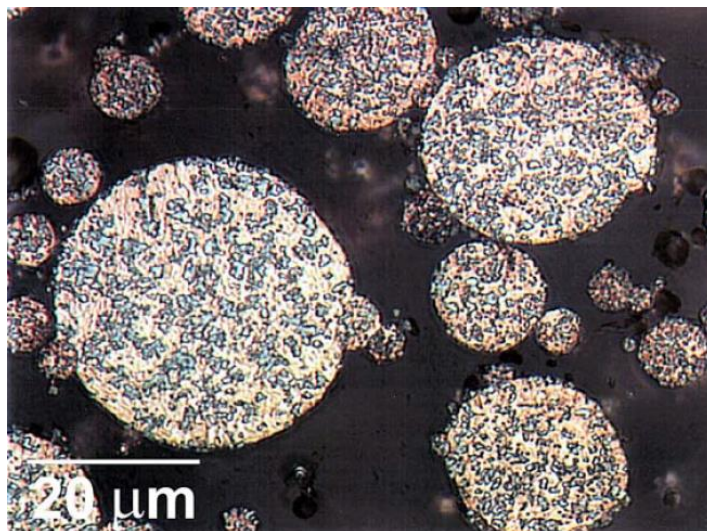


Figure 10: SEM image of GRCop-84 powder, a copper matrix containing 14 volume percent Cr_2Nb particles⁴.

The particles have extreme temperature stability up until 800°C, making them exceptional high temperature strengtheners (above this temperature particles begin to coarsen)⁴. This high temperature stability prevents their dissolution into solid-state copper, making the alloy unable to be solution hardened. Instead, the particles form exclusively during the liquid to solid transformation, requiring rapid cooling of the molten alloy to retain a small size. Slow cooling of either alloy through liquid-metal processes such as casting results in over-sized particles (~1cm diameter compared to the desired 1-5µm), resulting in poor strength and conductivity of the bulk material¹³. Thus, gas atomization of the molten alloy is used to rapidly cool individual droplets, resulting in a powder filled with fine Cr₂Nb particles. For operations that require solid material, GRCop powder can be consolidated through direct extrusion or HIPing of bulk powder, resulting in a fully dense solid form that can then be machined and worked as any copper alloy⁴. The development of powder-based manufacturing with this alloy has an obvious upside in this regard, not requiring the consolidation process.

GRCop-84 has already been used for the production of main combustion chamber liners using vacuum plasma spraying (VPS) as was seen in [Figure 4](#), having high temperature tensile properties comparable and better than other aerospace copper alloys including NARloy-Z, AmZirc, and GildCop AL-15. GRCop-84 was designed for high-temperature strength, having inferior low temperature yield strength in the HIPed condition, but retaining more strength at extreme temperatures as result of the stability of the particles ([Figure 11](#)).

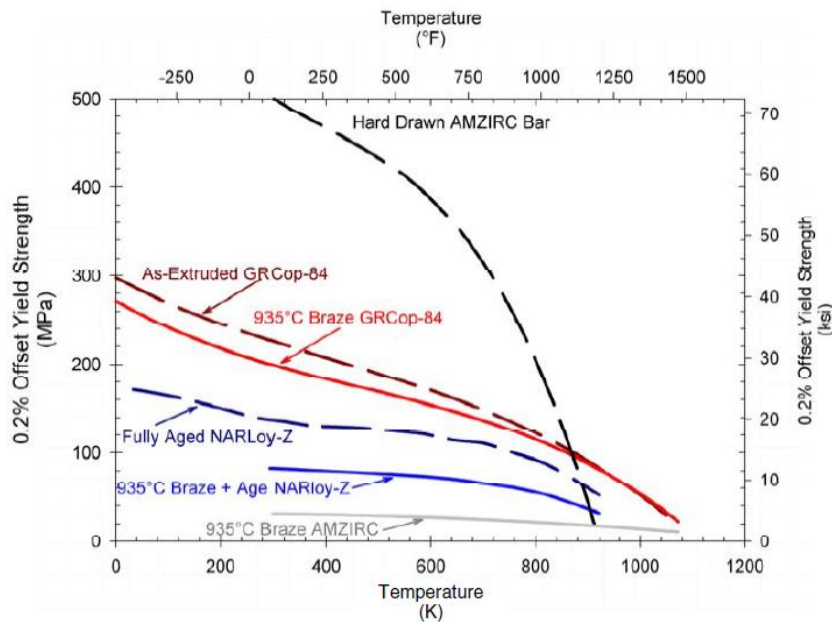


Figure 11: 0.2% offset yield strength of various aerospace copper alloys. As-consolidated and brazed GRCop-84 has a high retention rate of yield strength compared to competitors due to its strengthening phase being incredibly temperature stable¹⁴.

While GRCo-84 has mechanical properties superior to that of competing alloys, its thermal conductivity is low compared to other aerospace copper alloys across its operating temperatures. GRCo-42 on the other hand has greatly improved thermal conductivity compared GRCo-84 and competing alloys (Figure 12) while having the same strengthening mechanism as GRCo-84, and surprisingly nearly identical strength up to about 800°C, making it significantly higher than that of the current launch vehicle engine liner NARloy-Z⁶. While little work has been done on GRCo-42’s mechanical properties for comparison to other alloys, the importance of high thermal conductivity in MCC liners has driven the pursuit of GRCo-42 as a liner material. Previous work focused on the comparative low-cycle-fatigue life of GRCo-42 compared to GRCo-84 as well as the effects of heat treatment on the hardness of cold-sprayed samples of the powder material.

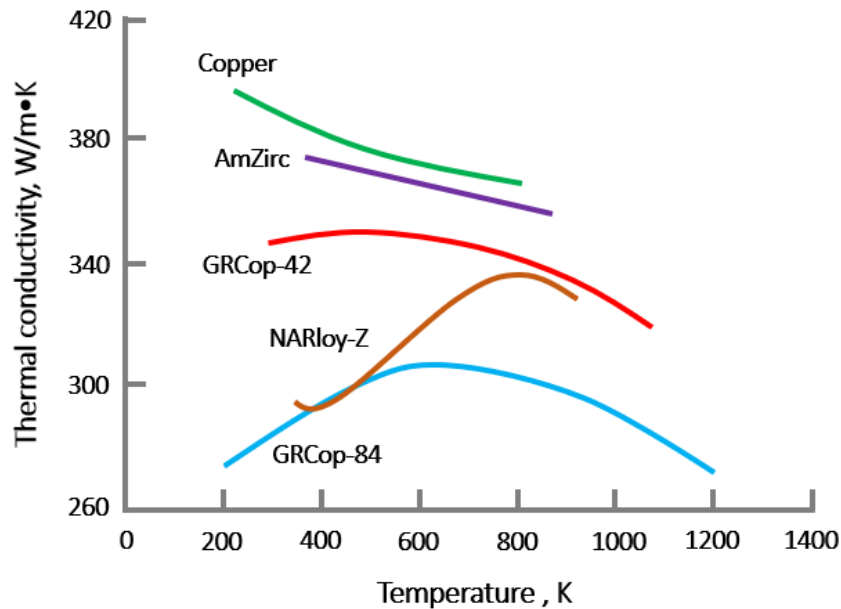


Figure 12: Plot of the comparison of thermal conductivity of various engineering copper alloys, highlighting the benefit of GRCo-42 over GRCo-84⁶.

As previously mentioned, the primary failure mechanism of main combustion chamber liners is low-cycle fatigue (LCF) due to the cyclic nature of thermal loading. Comparing the LCF life of GRCo-42, GRCo-84, and NARloy-Z show the statistically significant, but slim difference between the LCF life of the GRCo alloys, with GRCo-42 having nearly the same LCF life as NARloy-Z (Figure 13) with higher thermal conductivity across all relevant temperatures. The importance of thermal conductivity, LCF life, and strength retention at elevated temperature make GRCo-42 a potentially superior option for an MCC liner material compared to other alloys.

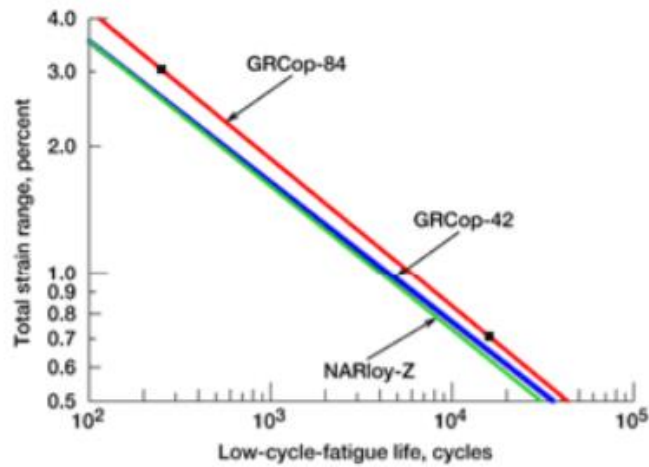


Figure 13: Comparison of the low-cycle-fatigue life of the GRCop alloys to NARloy-Z. Despite significantly higher thermal conductivity and nearly identical strengths, GRCop-42 has a nearly identical LCF life to NARloy-Z, only slightly reduced from GRCop-84⁶

When considering the application of GRCop-42 to cold spray additive manufacturing, the effect of heat treatment on the sprayed properties must be studied. Though limited, testing has been done on the effect of a two-hour annealing treatment of the sprayed materials hardness¹³. A short or low temperature annealing treatment allows for stress relief and strengthening of bonds, while treatments at higher temperature or for longer times will allow for significant grain growth. The effect of varying annealing temperature with constant time on the hardness of cold sprayed GRCop-42 is seen in [Figure 14](#).

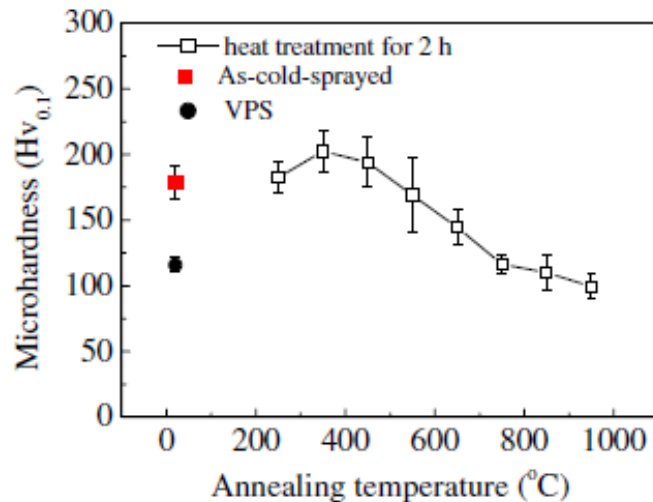


Figure 14: Effect of annealing treatments at a range of temperatures on cold-sprayed GRCop-42 microhardness. With low porosity, these trends will be roughly correlated to the effect on tensile strength and inversely so ductility¹³.

The peak in hardness at a lower annealing temperature supports the multi-step effect of heat treatment laid out in [Figure 9](#), with the lower temperature treatment not allowing for full recrystallization and maintaining of strength, where high temperature treatments caused grain growth and increased ductility. Assuming low porosity, as is typical for cold sprayed copper alloys with their low specific strength¹², the trends in tensile properties can be compared to that of the hardness. As such, achieving practical mechanical properties for a cold-sprayed GRCop-42 component is entirely feasible, and a heat treatment path can be developed for the ideal properties of an MCC liner or any other component.

1.4 Problem Statement

Cold-spray additive manufacturing (CSAM) is a manufacturing method desirable for its speed, ability to produce complex shapes, and lack of required investment into often-costly dies or molds. As such manufacturers want to apply CSAM to small-batch components that are currently manufactured with either expensive or wasteful techniques. One of these small-batch components is the main combustion chamber (MCC) liner of rocket engines, typically composed of an advanced copper alloy for their high thermal conductivity, mechanical property retention at high temperatures, and low-cycle-fatigue life. GRCop-42 is one such copper alloy that meets the mechanical and thermal property requirements while being a powder alloy, convenient for cold-spray manufacturing. However, the poor as-manufactured ductility of cold-sprayed components inhibit low-cycle-fatigue life, requiring a heat treatment to increase ductility and make CSAM a viable manufacturing technique. To determine whether cold-sprayed GRCop-42 could be a viable alloy-manufacturing pair for MCC liners we seek to determine the effect of annealing heat treatment on its tensile properties. Hardness of heat treated CSAM GRCop-42 will be studied alongside the resulting microstructural features as a precursor to the more relevant fatigue and thermal properties that qualify GRCop-42 as an MCC material. Testing methods for this project include hardness testing, optical microscopy, scanning electron microscopy, and particle counting of multiple samples of cold-sprayed GRCop-42.

2. Experimental Procedure

2.1 Heat Treatments and Sample Preparation

Two samples of cold-sprayed GRCop-42 were provided by Aerojet Rocketdyne, each with a different set of cold-spray parameters and designated as either 2B or 3C (Figure 15). For ease of manufacturing, GRCop-42 powder was cold-sprayed onto an aluminum substrate. Initial sections were cut from each sample using a precision-cut-off saw for reference data in the as-sprayed condition. The remaining sample was shipped back to Aerojet Rocketdyne where the aluminum substrate was removed, and each sample underwent a hot-isostatic pressing (HIP) treatment at 1750°F and 15ksi for two hours before being shipped back to Cal Poly SLO. The solid-copper samples were then cut into three sections each, two of which were preserved in the as-HIPed condition. The remaining four samples were divided into two treatment groups, with one of each type being vacuum annealed at 1700°F and the other at 1800°F. Each treatment lasted for one hour and was followed by a nitrogen gas back-fill cooling. Treatments are summarized in Table I.

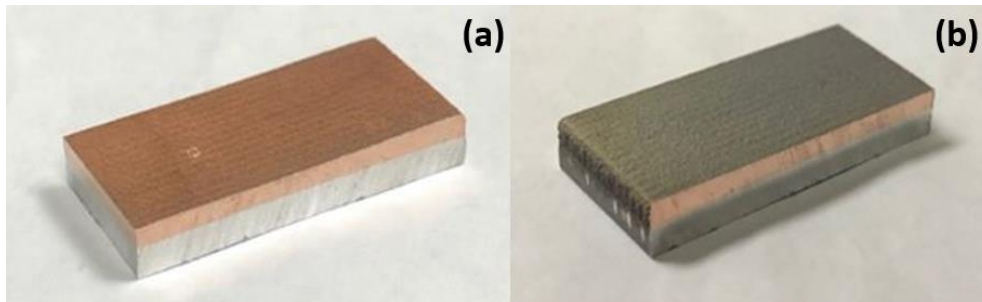


Figure 15: As-sprayed samples of cold-sprayed GRCop-42 (a) 2B and (b) 3C. Each designation denotes a different set of confidential cold-spray parameters.

Table I: Summary of Sample Designations and Their Treatments

Cold Spray Parameters / Treatment	2B	3C
As-sprayed	2B-AS	3C-AS
As-HIPed	2B-HIP	3C-HIP
HIPed + 1hr 1700°F anneal	2B-17	3C-17
HIPed + 1hr 1800°F anneal	2B-18	3C-18

2.2 Microhardness Testing

Microhardness was performed after fine polishing and before etching in accordance to ASTM E384¹⁵.

Five micro-indentations were made in various locations across the surface, at least 2.5 times the size of the indentation apart. The extreme variance in hardness between samples necessitated the use of multiple force values for the hardness calculation. Hardness was calculated using Eq, where d_x and d_y are in millimeters and load is in grams.

$$HV = 0.1891 \times 9.81 \left[\frac{m}{s^2} \right] \times \frac{Load[g]}{1000 \left(\frac{\frac{d_x + d_y}{2} [mm]}{1000 \left[\frac{mm}{m} \right]} \right)^2} \quad \text{Eq.1}$$

2.3 Optical and Scanning Electron Microscopy

Samples were each mounted in Bakelite, oriented such that the transverse plane was exposed: this was done to best reveal the cross section of the powder interfaces in the direction they were sprayed (Figure 16). GRCop-42 powder was mounted using a thermoset acrylic by adding the mounting polymer on top of a small amount of powder than rested at the bottom of the mold. The same polishing procedure was done for powder as solid material.

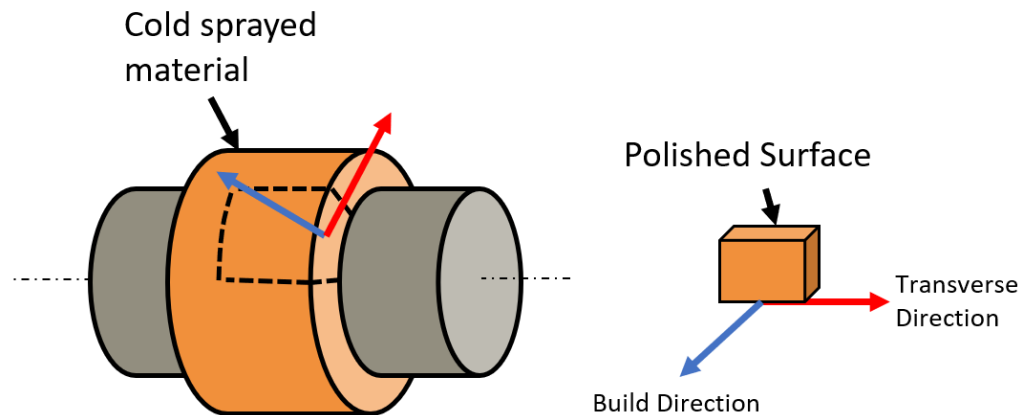


Figure 16: Diagram of sample geometry referencing the build direction.

Mounted samples were rough polished on 240, 360, 480, 600, 800, and 1200 grit abrasive paper. Initial trials without the two finest grits resulted in the presence of deep scratches remaining on the surface even

after fine polishing. Polishing was done on an Allied “Final P” pad designed for copper and aluminum alloys using 6 μ m and 1 μ m glycol-based diamond suspension until a scratch free surface was obtained.

Solid samples were etched using ferric-chloride etchant. Only a portion of the surface was etched so that the etched and unetched structures could both be observed without the need to re-etch or re-polish.

Etching was done until a cloudy appearance was seen on the previously mirrored surface of each sample, ranging from 5-15 seconds, with the as-sprayed samples requiring the most time for a desirable etch.

Powder samples were not etched.

SEM preparation included the standard cleaning in a bath of acetone in an ultrasonic cleaner for five minutes. Copper tape was wrapped from the surface of each sample to the bottom of the mount to form a conductive path to the SEM sample holder.

2.4 Safety

Proper lab safety procedures were followed for each process performed. Eye protection, closed toe shoes, and long pants were always worn in lab. While performing chemical etching, additional personal protective equipment was worn, including chemical goggles, nitrile gloves, and an apron. All etching was done within a fume hood and acid waste properly disposed of into the acidic etchant container.

3. Results

3.1 Optical Microscopy

3.1.1 Etched Surfaces

Optical microscopy was performed on each sample, with representative 500x magnification micrographs revealing the transformation of the microstructure. High contrast grain boundaries (**Figure 17**) become less dark with HIPing treatment (**Figure 18**) before not having any contrast after annealing at either treatment temperature (**Figure 19**, **Figure 20**).

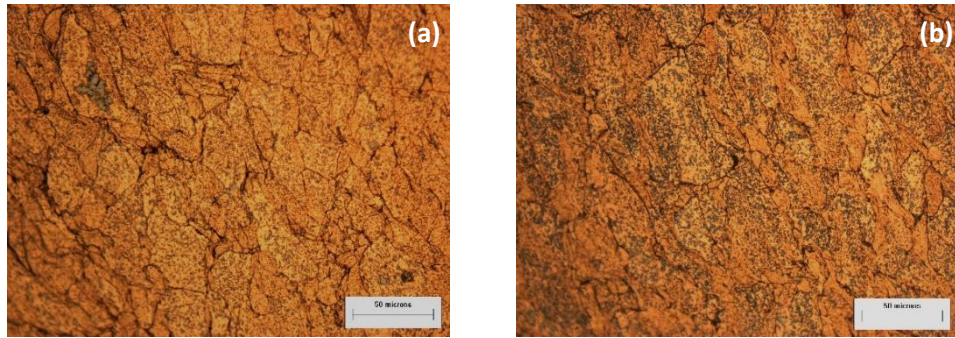


Figure 17: Etched micrographs of sample (a) 2B and (b) 3C in the as-sprayed condition reveal preferentially etched grain boundaries and clearly visible Cr_2Nb particles.

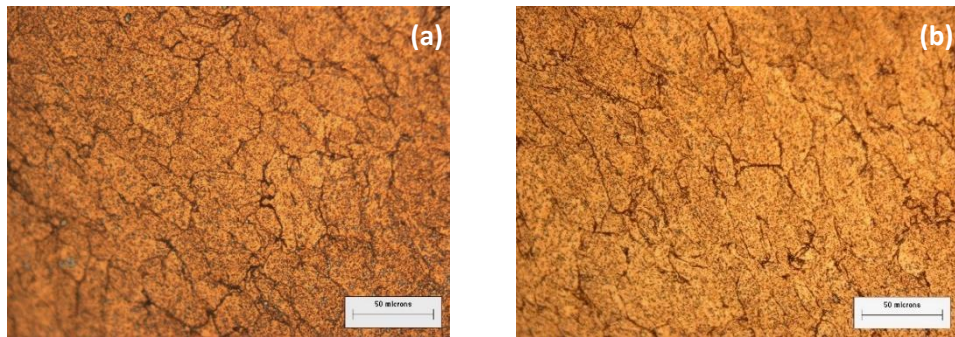


Figure 18: Etched micrographs of sample (a) 2B and (b) 3C in the HIPed condition have reduced darkening of grain boundaries compared to the as-sprayed samples.

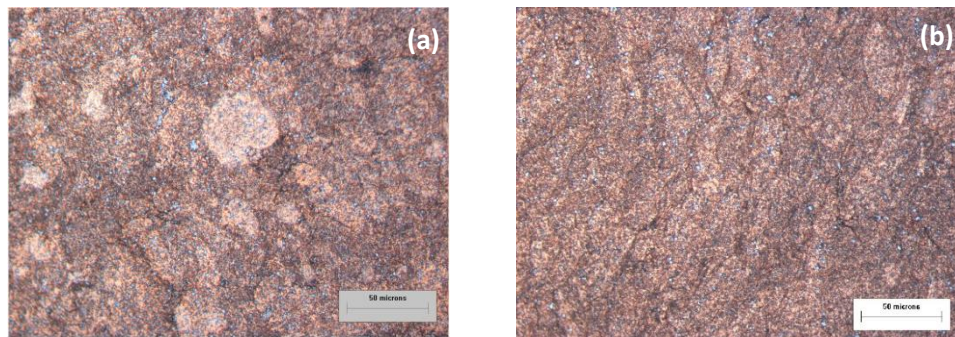


Figure 19: Etched micrographs of sample (a) 2B and (b) 3C after a 1700°F anneal no longer show significant contrast at grain boundaries, instead having a more uniform etch.

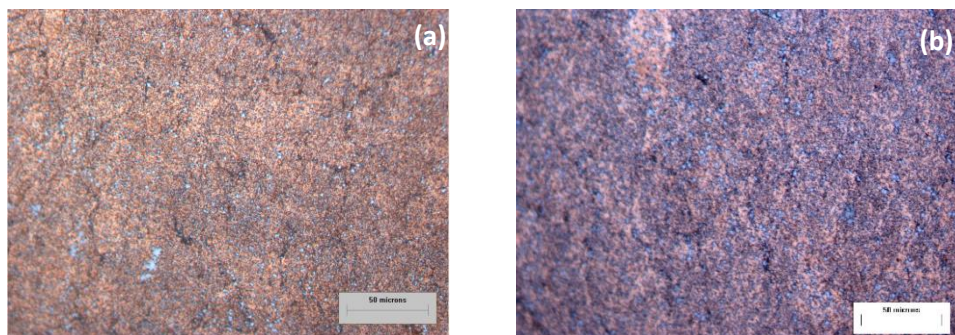


Figure 20: Etched micrographs of sample (a) 2B and (b) 3C after a 1800°F anneal show the same uniform etch as seen in the 1700°F anneal.

3.1.2 Powder Microscopy

Optical microscopy was performed on mounted powder to observe the size and distribution of Cr₂Nb particles prior to being sprayed. During the polishing process, particles over a certain diameter were ripped from the surface, leaving medium and small sized powder. Only medium size powder particles were documented due to microscope limitations (**Figure 21**). Deviation between Cr₂Nb particle size and their distribution within the copper matrix can be seen prior to any processing.

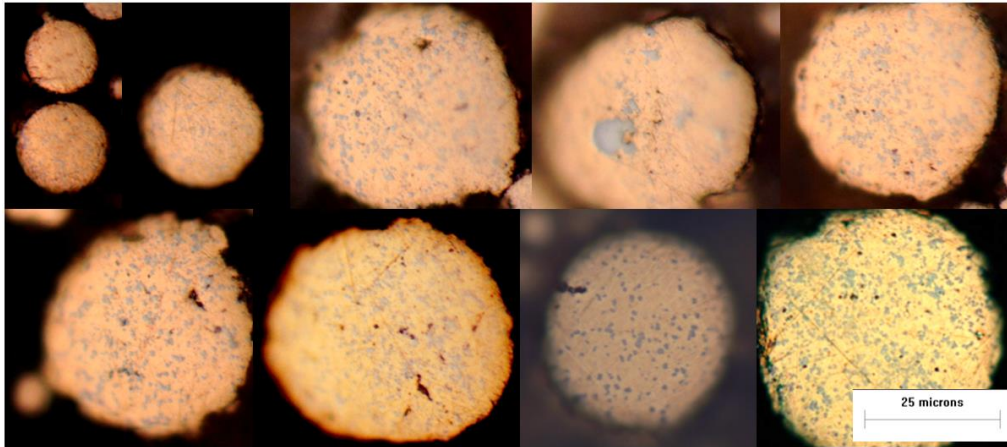


Figure 21: Compilation of 1000x magnification micrographs of powder particles. Cr₂Nb particles within are clearly visible in the unetched condition.

3.2 Microhardness Data

Five indentations were made in each sample and the x- and y-dimensions of each indentation were recorded for sample 2B (**Table II**) and sample 3C (**Table III**). Different loads were used due to the significant difference in hardness, while this potentially effected the results, the use of higher loads minimized the potential error. Using **Eq 1** the hardness of each sample was calculated in Vickers.

Table II: Indentation Size and Resulting Microhardness Data for Sample 2B

Sample ID	2B-AS		2B-HIP		2B-17		2B-18	
Force (g)	2000		2000		500		500	
1 (μm)	140	133.5	89	89	100	103	110.5	111.5
2 (μm)	144	144	90.5	91	110.5	116	117	117.5
3 (μm)	142.5	140	92	92.5	106.5	108	105.5	106
4 (μm)	139	138	94	96	112.5	113.5	109	111
5 (μm)	142	141	83.5	84.5	104.5	106	113	114.5
Avg. Hardness (HV)	188.4		114.3		79.9		74.8	
St. Dev (HV)	7.6		10.2		7.6		5.8	

Table III: Indentation Dimensions and Resulting Microhardness Data for Sample 3C

Sample ID	3C-AS		3C-HIP		3C-17		3C-18	
Force (g)	2000		2000		500		500	
1 (μm)	133	134	86	86	106	107.7	93.5	96
2 (μm)	134.5	139	84.5	85.5	104	105	100.5	102.5
3 (μm)	135	131.5	94.5	93.5	99	101.5	98.5	99.5
4 (μm)	131	138	84.5	83	92.5	95	96	97.5
5 (μm)	135.5	130	86.5	86	102	103.5	93	95
Avg. Hardness (HV)	206.2		123.1		90.4		98.4	
St. Dev (HV)	4.8		10.6		9.4		6.2	

The resulting microhardness data was plotted (Figure 22), showing a clear trend of hardness reducing with increasing treatment duration and a difference between the cold-spray processing parameters. Despite these trends being evident, statistical analysis is needed to make any assertions.

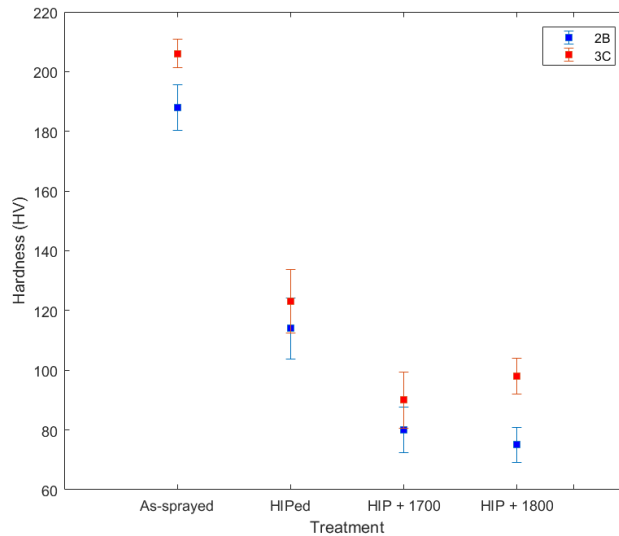


Figure 22: Plot of microhardness vs treatment for each cold-sprayed sample, showing a relationship between increased heat treatment duration and reduced microhardness. Statistical analysis is needed to determine the significance of any differences.

3.3 Scanning Electron Micrographs

3.3.1 Surface Analysis

SEM analysis was performed to give additional context to the surface morphology of the samples. The samples being polished to a mirror finish makes the final images less indicative of properties than a fracture surface, but a few theories could still be made, namely the progression of grain boundary etching and the visibility of Cr_2Nb particles. The image of the as-sprayed surface (Figure 23) reveals the extent of the deformation present after the cold-spray process, with grains being deformed significantly from their

initial spherical shape. Despite etching, and their visibility in optical microscopy, no Cr_2Nb particles are seen.

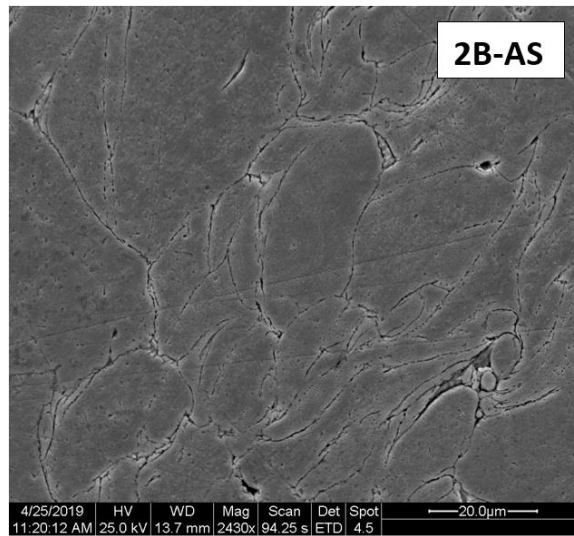


Figure 23: The etched surface of sample 2B-AS with grain boundaries being etched preferentially. Signs of porosity and increased deformation in some areas are also present.

The surface of the HIPed sample shows significant amounts of Cr_2Nb particles within the structure (Figure 24), with particles clearly seen as surrounding grains to prevent their growth. However, with the additional annealing heat treatment (Figure 25) the strengthening particles are no longer visible as they were in the HIPed surface. The primary difference post-annealing is the reduced contrast of the grain boundaries and the possible increased degree of etch across the sample's surface.

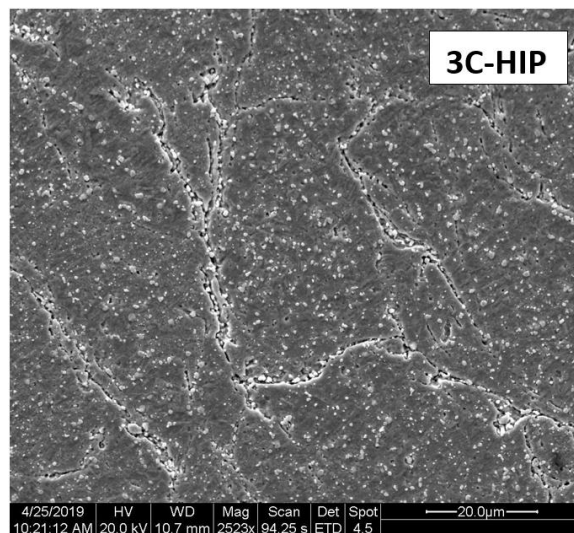


Figure 24: Etched surface of sample 3C-HIP reveals grain boundaries and Cr_2Nb particles that lie within and between them.

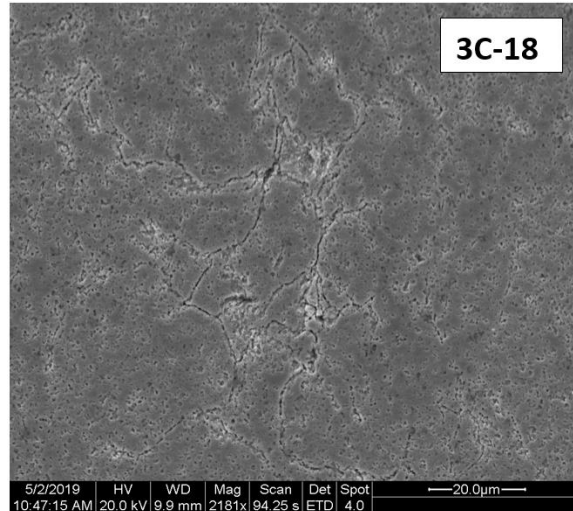


Figure 25: Etched surface of sample 3C-18 reveals some etching of grain boundaries, but primarily the etching of the surface.

3.3.2 Oxide Analysis

Energy-dispersive x-ray spectroscopy (EDS) was conducted to gain insight into the composition of multiple oxides present on the surface of the cold-sprayed samples. Initial SEM examination revealed multiple oxides present in a representative area (Figure 26) and multiple oxides were sampled to determine their compositions, including a bright oxide (Figure 27), a dark oxide (Figure 28), and two adjacent grey oxides (Figure 29). EDS of these oxides suggests two compositions present.

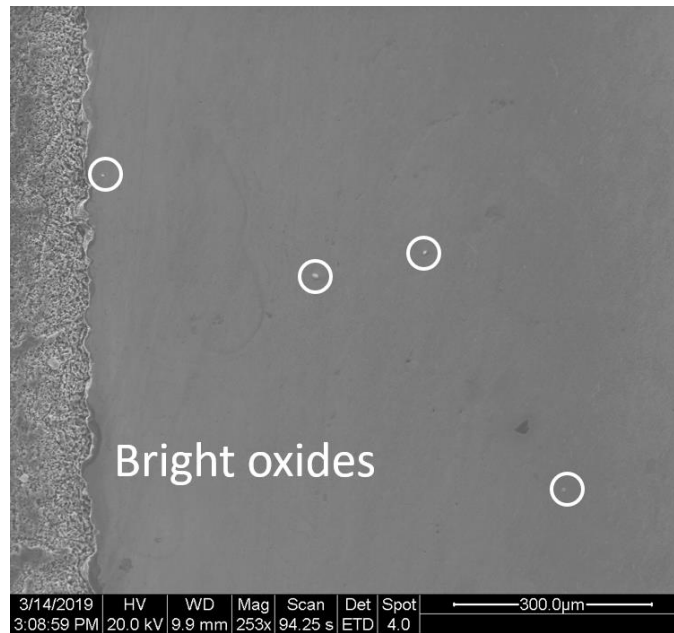


Figure 26: SEM image depicting multiple oxides on the surface of sample 2B-AS.

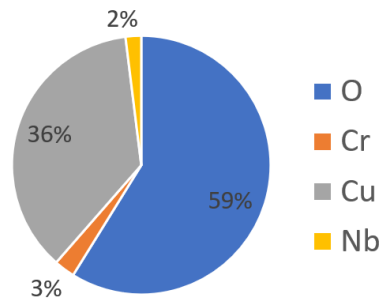
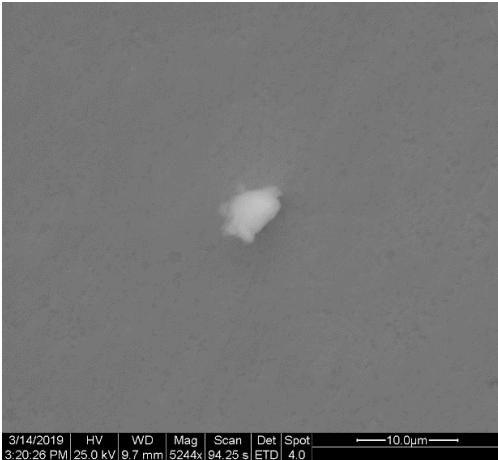


Figure 27: SEM image and composition of an oxide present on the surface of sample 2B-AS, with results not containing any unexpected elements and likely being a copper-based oxide.

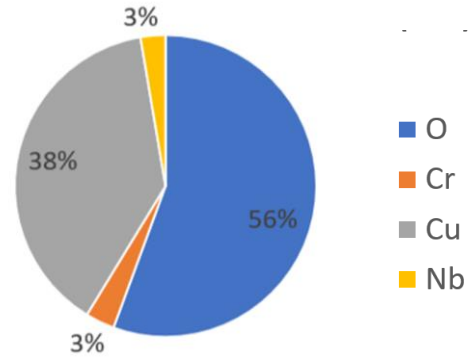
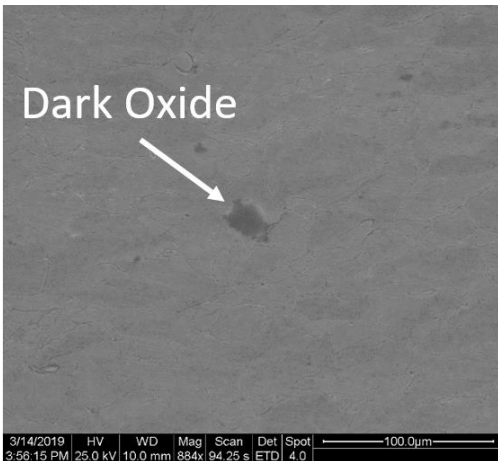


Figure 28: SEM image of a dark oxide from sample 2B-AS shows a visual difference from the oxide in Figure 23, but compositionally the two are likely identical.

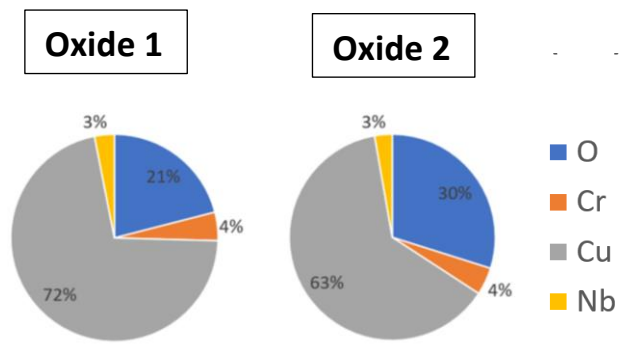
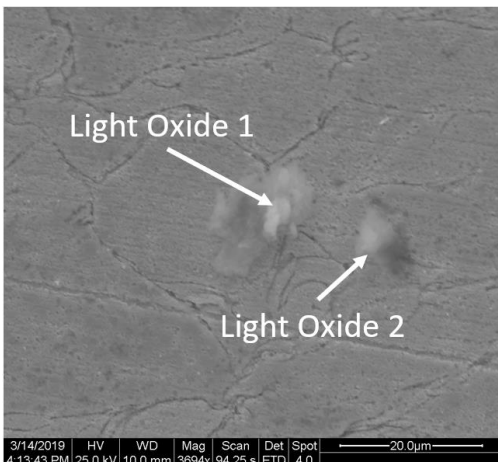


Figure 29: EDS analysis of two adjacent oxides reveals similar compositions that are different than those sampled in Figure 23 and Figure 24.

3.4 Particle Size Distributions

Particle size distributions were measured to determine whether each stage of heat treatment had a significant effect on the size of Cr₂Nb particles. Due to a poor contrast between particle and matrix in a majority of the taken SEM images and all the optical micrographs, the software ImageJ was inaccurate and not used. Instead particles were measured manually: while a new source of human error was introduced, any foreign bodies could be more easily ignored. Over 100 particles were measured from each sample in groups 2B and 3C, with their diameters grouped and the occurrence of each range put into bar charts in **Figure 30**. The non-normal shape of the distributions is also expressed through comparisons of the mean and median values of each size distribution listed in **Table IV**, with the significant differences also suggesting non-normality. For a more representative view of the data, the median size values were plotted in **Figure 31** for a quantitative view of the results, with the error associated from manual measurements leading to high standard deviations relative to particle sizes.

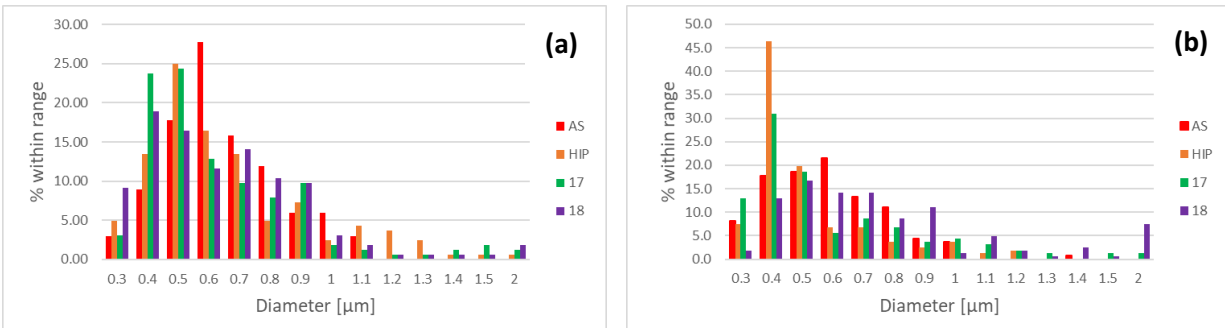


Figure 30: Particle size distributions for sample (a) 2B and (b) 3C shows a non-normal distribution, instead being right skewed. The shape of the distributions indicates that ANOVA cannot be used.

Table IV: Mean, Median, and Standard Deviation of Particle Diameters in Sample Groups 2B and 3C

Cold Spray Parameters / Treatment		2B	3C
AS	Mean	.607	.558
	Median	.581	.540
	St. Dev	.186	.240
HIP	Mean	.620	.471
	Median	.538	.387
	St. Dev	.270	.201
17	Mean	.587	.539
	Median	.494	.419
	St. Dev	.269	.295
18	Mean	.608	.744
	Median	.538	.645
	St. Dev	.301	.403

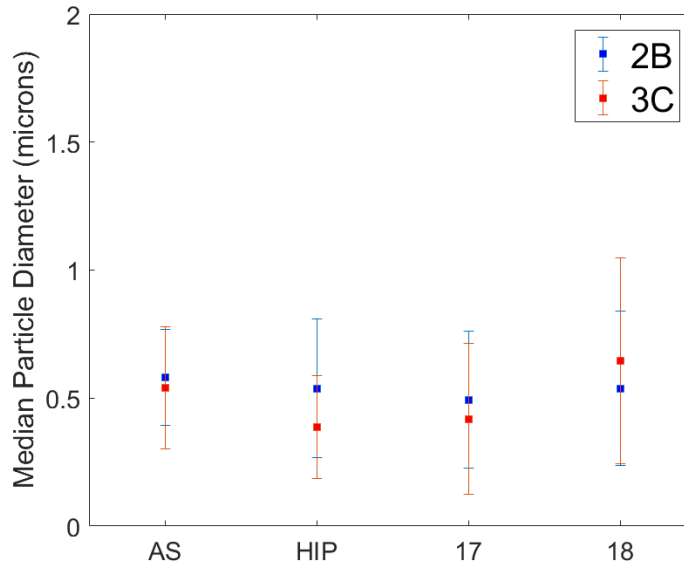


Figure 31: Plot of the median particle diameter for each sample across all treatment levels. High error due to manual measurement likely influenced the high standard deviation.

4. Discussion

4.1 Optical Microscopy

Comparison of optical micrographs of etched surfaces across treatment levels suggests multiple possible property and structure changes. The most evident trend is the reduced contrast of grain boundaries with increasing heat treatment duration. There are multiple possible effects causing this change, primarily caused by increased levels of diffusion: mechanical bonded powder particles are ‘bridged’ on the atomic scale, recrystallization relieving dislocations bunched at grain boundaries, boundary energy reduction, particle growth, and others. These changes have significant potential implications on the resulting thermal and mechanical properties of the material including increased thermal conductivity¹⁶, fracture toughness, and most importantly, low-cycle fatigue life.

Microscopy on the unetched powder shows deviation between the size and spread of Cr₂Nb particles within untreated powder. This will affect the resulting sprayed structure and must be considered when measuring particle size distributions.

4.1.1 Possible Effect on Fracture Toughness and LCF life

Diffusion bridging the powder boundaries has a significant effect on the strength of the resulting bulk material¹³. Grains being bridged by diffusion reduces the effective porosity of the material as mechanical

boundaries can begin to seal¹². In addition to the boundaries being fused by diffusion, their energy is also likely reduced due to the recrystallization and relieving of bunched dislocations that occurs during heat treatment¹². This lowering of boundary and strain energy shifts the energy balance of crack growth to require higher stresses for crack propagation. These two effects, gap closing and boundary energy decreasing, act together to increase the fracture toughness of the material, increasing the required critical flow size and the stress for unstable crack propagation.

4.1.2 Possible Effect on Thermal Conductivity

Previous literature suggests that the heat treatment increases the thermal conductivity of cold-sprayed copper alloys through closing of former powder boundaries and stress relief. This effect has diminishing positive effects, as beyond a critical annealing temperature, voids not closed during treatment will rearrange at grain boundaries and decrease thermal conductivity. The evident reduction in grain boundary energy from the optical microscopy results suggests an increase in thermal conductivity post-annealing treatment. However, with GRCop-42 there is the added effect of particle coarsening potentially reducing thermal conductivity so no definite claims can be made.

4.2 Microhardness

While an obvious trend is present between increased heat treatment duration and reductions in microhardness, statistical analysis was required to determine whether the varying cold-spray parameters (2B, 3C) and processing parameters (-AS, -HIP, -17, -18) had a statistically significant effect on the resulting microhardness. To determine whether ANOVA was an appropriate statistical method, a normality test was conducted on the microhardness data ([Figure 32](#)).

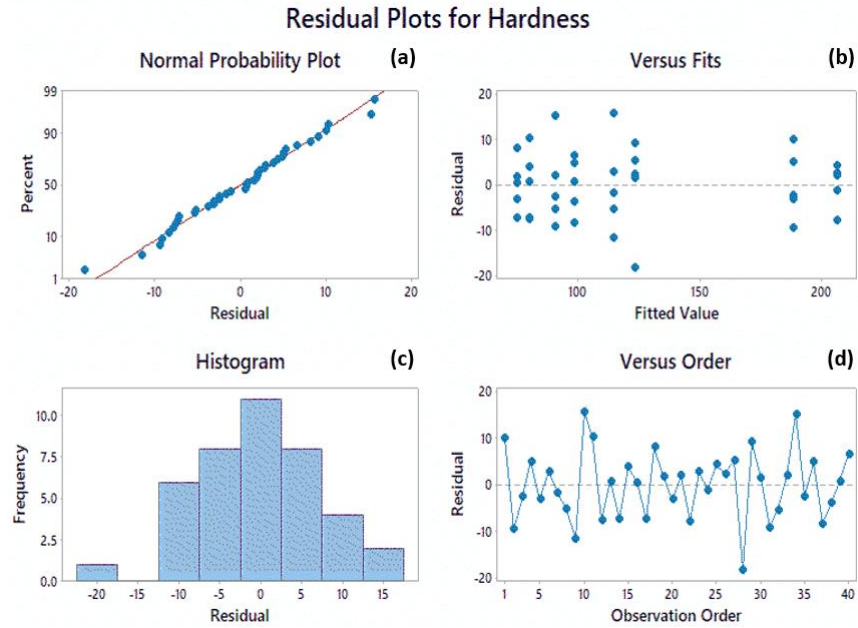


Figure 32: (a) Microhardness value clearly follows a normal distribution, with no significant non-linearity of the residuals. (b) Versus fits shows the even distribution around a residual of 0, indicating that there were no effects that would require a transformation of the data to meet ANOVA requirements. (c) Is a visual representation of the normal distribution and (d) versus order shows the randomness of the data with no evident skews.

Resulting analysis shows the data to be normally distributed and random, qualifying ANOVA for further comparisons. With two factors being present within the group of samples, referred to as ID and Process, multi-factor ANOVA needed to be conducted. First however, the significance of each factor in addition to their interaction (ID*Process) was determined (Table V). The P-value being above 0.05 for the interaction deemed it insignificant and was not included for the multi-factor ANOVA mean effects plot (Figure 33).

Table V: ANOVA Test Results Determining the Significance of Each Factor

Source	DF	Adj SS	Adj MS	F-Value	P-Value
ID	1	2309.9	2309.9	36.02	0.000
Process	3	82957.2	27652.4	431.22	0.000
ID*Process	3	349.6	116.5	1.82	0.164
Error	32	2052.1	64.1		
Total	39	87668.7			

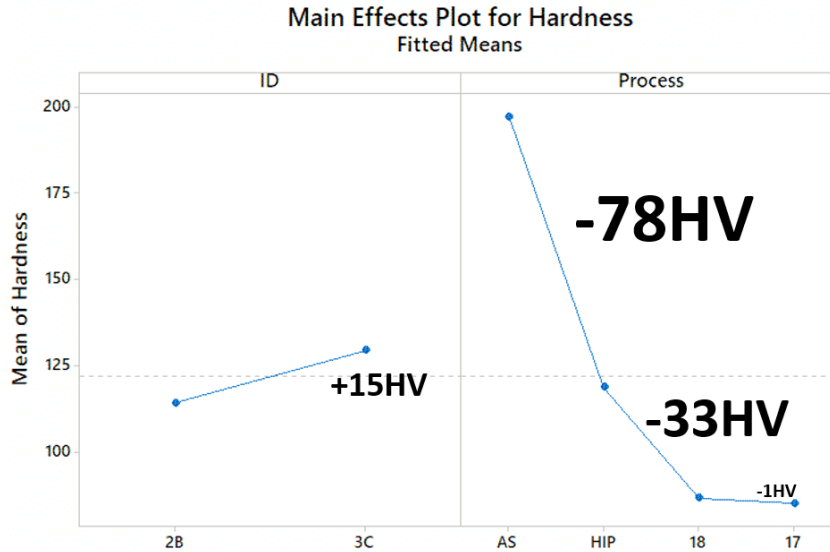


Figure 33: Analysis of the effect of each factor, being ID or Process, shows that sample 3C is statistically significantly harder than sample 2B. Comparing the different processing methods, as-sprayed is the hardest and is different than HIP, and HIP is harder and different than -17 and -18. There is no significant microhardness difference between the -17 and -18 treatments.

Significant reductions occurring after both the HIP and annealing treatments suggests multiple hardness-reducing factors at play. Copper recrystallizes fairly quickly, and as such it is possible that recrystallization completed during the HIP treatment and the annealing treatment reduced hardness through particle coarsening. Grain boundary growth is unlikely due to the boundary-pinning by the Cr_2Nb particles. Optical microscopy results suggest that powder boundaries still had dislocations present with the preferential etch of boundaries. Lack of data does not allow for any definite sources of hardness reduction, but statistical analysis of the reductions does allow for qualitative conclusions to be made.

4.3 SEM

Analysis of a polished surface does not allow for as rigorous of conclusions to be made as analysis of fracture surfaces, but some possible effects can still be noted. The HIPing treatment appeared to be the ideal etched surface condition, with both grain boundaries and particles clearly being seen. From [Figure 24](#) it is evident that the Cr_2Nb particles surround grains and likely prevent their growth due to their high thermal stability. For this reason, grain size was not measured within this research, supported from decisions from prior literature. The primary difference that is seen between the three stages of treatment is the regions that appear to be preferentially etched: as-sprayed etches mostly at the boundaries, HIPed

etches around both particles and boundaries, and annealed samples appears to etch across the entire surface.

EDS results give a baseline dataset that can be referenced in future work but do not provide enough information for conclusions on their own. Results do suggest that there are multiple compositions of oxides present on the surface, one being primarily copper and the other primarily oxygen but each with only trace amounts of chromium and niobium. The low concentrations of these alloying elements suggest a high degree of purity of the copper matrix, as little to none of the elements were free to form their own oxides. A pure matrix has positive implications for the thermal properties, as pure copper has higher thermal conductivity than copper with an alloying element in solid solution.

4.4 Particle Size Distributions

The non-normal shape of the particle size distributions seen in [Figure 30](#) disqualifies ANOVA as a statistical analysis technique. Even when the raw particle-size data was transformed to a log-base-ten scale, normality tests failed for each group. As such, non-parametric statistical analysis was conducted, with the requirements for valid analysis not including a normal distribution. Each distribution meets the requirements of the same shape (right skewed) and similar variance. With the relevant comparison being within each group of the same cold-spray parameters, non-parametric Kruskal-Wallis analysis was performed for groups 2B and 3C ([Table VI](#), [Table VII](#)) to determine whether each heat treatment had a significant effect on the median particle diameter. A P-value above 0.05 indicates no significant difference in means across any heat treatment level.

Table VI: MiniTAB Output for Sample 2B Non-Parametric Comparison

Kruskal-Wallis Test: Size 2B versus Type 2B

Descriptive Statistics

Type 2B	N	Median	Mean Rank	Z-Value
2B-17	164	0.494624	279.7	-1.52
2B-18	164	0.537634	289.4	-0.66
2B-AS	101	0.580645	326.1	1.87
2B-HIP	164	0.537634	304.0	0.62
Overall	593		297.0	

Test

Null hypothesis H₀: All medians are equal
 Alternative hypothesis H₁: At least one median is different

Method	DF	H-Value	P-Value
Not adjusted for ties	3	5.18	0.159
Adjusted for ties	3	5.19	0.159

Table VII: MiniTAB Output for Sample 3C Non-Parametric Comparison

Kruskal-Wallis Test: Size 3C versus Type 3C

Descriptive Statistics

Type 3C	N	Median	Mean Rank	Z-Value
3C-17	162	0.419355	276.5	-2.85
3C-18	162	0.645161	402.3	7.53
3C-AS	135	0.540000	323.7	0.93
3C-HIP	162	0.387097	243.6	-5.57
Overall	621		311.0	

Test

Null hypothesis H₀: All medians are equal
 Alternative hypothesis H₁: At least one median is different

Method	DF	H-Value	P-Value
Not adjusted for ties	3	71.51	0.000
Adjusted for ties	3	71.53	0.000

Results show that group 2B had no significant change in median particle diameter across any treatment level, whereas 3C had at least one median that was significantly different. To determine which of the medians were different, individual Mann-Whitney tests were run between relevant comparisons: 3C-AS to 3C-HIP, 3C-HIP to 3C-17, 3C-HIP to 3C-18, and 3C-17 to 3C-18. Results of those statistical analyses were mixed: no coarsening was evident between 3C-HIP and 3C-17 but was present between 3C-HIP and 3C-18 to the extent that 3C-18 was also statistically larger than 3C-17. Most interestingly, 3C-AS had a statistically higher median particle size than 3C-HIP, suggesting a possible shrinking of particles with the HIP treatment.

Growth-rate kinetics deems the shrinking of particles given increased thermal energy unlikely and this conclusion makes the entirety of the particle size results questionable. Analysis of the as-sprayed microstructure ([Figure 34](#)) suggests natural variance in Cr₂Nb particle size significantly skewing results depending on the samples' area. Different particle sizes can be clearly observed between adjacent former powder particles. Any hand-counted representative area coupled with low-resolution micrographs makes results inaccurate, as an accurate distribution would require a significantly larger sampled area and inclusion of the particles currently 'lost' to low resolution.

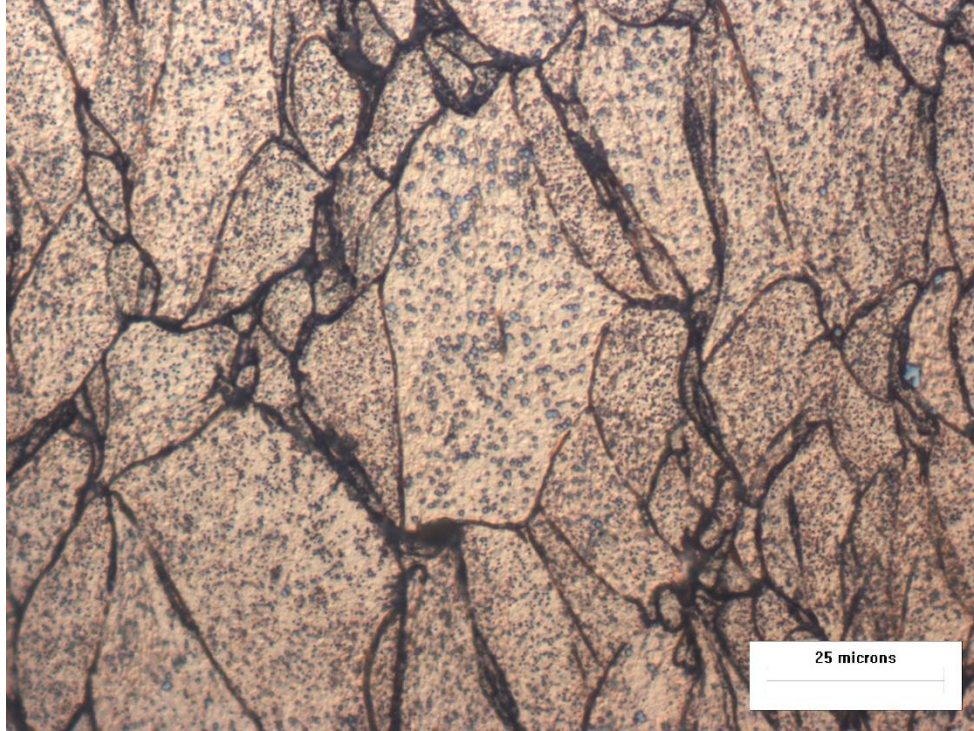


Figure 34: Sample 2B-AS at 1000x magnification shows the natural variance of Cr_2Nb particles within the as-sprayed structure. Hand-counting particles can result in widely different size distributions depending on the area sampled.

As such, results from particle hand-counting was inconclusive due to limited equipment and the large representative areas required.

5. Conclusions

1. HIPing and annealing had the most significant impact on microhardness, reducing average hardness by 78HV and 33HV, respectively, followed by cold-spray processing parameters, where 3C had an average hardness 15HV higher than 2B.
2. The 100°F-annealing temperature difference did not significantly affect resulting microhardness, with an average hardness difference of 1HV.
3. Oxides sampled on the sample surface possibly had one of two compositions, being primarily copper or oxygen with trace amounts of chromium and niobium.
4. Low alloying element concentration in oxides suggests a low amount of chromium and niobium in the copper matrix.
5. Particle size distributions could not be accurately measured due to low resolution micrographs and small sample regions possible with manual counting and measuring.

6. Recommendations

1. Redo particle counting on the unetched surface of samples with a higher resolution microscope and particle counting software to allow for larger sampled regions and more accurate size distributions.
2. Higher accuracy EDS on more surface oxides and the copper matrix to gain further insight into the effects of oxides on properties and determine the purity of the matrix.
3. Any further testing of cold-sprayed GRCop-42 include samples from processing parameters 2B and 3C, as their hardnesses are different enough that other properties could also vary.

7. References

- [1] L. Hutchinson, "How NASA brought the monstrous F-1 'moon rocket' engine back to life - Ars Technica." [Online]. Available: <https://arstechnica.com/science/2013/04/how-nasa-brought-the-monstrous-f-1-moon-rocket-back-to-life/>.
- [2] A. Rocketdyne, "AR1 Booster Engine - Aerojet Rocketdyne." [Online]. Available: <http://www.rocket.com/ar1-booster-engine>.
- [3] T. Benson, "Liquid Rocket Engine." [Online]. Available: <https://www.grc.nasa.gov/www/k-12/rocket/rockth.html>.
- [4] D. L. Ellis, *Aerospace Structural Materials Handbook Supplement 1 General I. I Commercial Designation*. Cleveland, 2018. [Online]. Available: <https://ntrs.nasa.gov/search.jsp?R=20020070630>
- [5] M. Fassin, S. Wulfinghoff, and S. Reese, "Modelling Thermal Barrier Coatings and Their Influence on the Lifetime of Rocket Engine Nozzle," no. January, 2016.
- [6] N. Glenn, S. Shuttle, M. Engine, W. Rl-, and T. Grcop-, "Conductivity of GRCop-42 Alloy Enhanced," 2019. [Online]. Available: <https://ntrs.nasa.gov/search.jsp?R=20050192166>
- [7] "NASA Relies on Copper for Shuttle Engine," Standards & Properties: Metallurgy of Copper-Base Alloys. [Online]. Available: https://www.copper.org/publications/newsletters/discover/1992/Ct73/shuttle_engine.html.
- [8] S. Yin *et al.*, "Title: Cold spray additive manufacturing and repair: Fundamentals and applications Cold spray additive manufacturing and repair: fundamentals and applications," *Addit. Manuf.*, vol. 21, no. 17, pp. 30299–3, 2018.
- [9] H. Assadi, F. Gärtner, T. Stoltenhoff, and H. Kreye, "Bonding mechanism in cold gas spraying," *Acta Mater.*, vol. 51, no. 15, pp. 4379–4394, 2003.
- [10] F. Meng, S. Yue, and J. Song, "Scripta Materialia Quantitative prediction of critical velocity and deposition efficiency in cold-spray : A finite-element study," *Scr. Mater.*, vol. 107, pp. 83–87, 2015.
- [11] D. L. Gilmore, R. C. Dykhuizen, R. A. Neiser, T. J. Roemer, and M. F. Smith, "Particle Velocity and Deposition Efficiency in the Cold Spray Process," vol. 8, no. December, pp. 576–582, 1999.
- [12] R. Huang, M. Sone, W. Ma, and H. Fukanuma, "Surface & Coatings Technology The effects of heat treatment on the mechanical properties of cold-sprayed coatings," *Surf. Coat. Technol.*, vol. 261, pp. 278–288, 2015.
- [13] W. Li, X. P. Guo, C. Verdy, L. Dembinski, H. L. Liao, and C. Coddet, "Improvement of Microstructure and Property of Cold-Sprayed Cu – 4 at .% Cr – 2 at .% Nb alloy by Heat Treatment," vol. 55, pp. 327–330, 2006.

- [14] D. L. Ellis, "GRCop-84 : A High-Temperature Copper Alloy for High-Heat-Flux Applications," no. February 2005, 2018.
- [15] ASTM Standard E384, 2016, "Standard Test Method for Microindentation Hardness of Materials," ASTM International, West Conshohocken, PA, 2003, DOI: 10.1520/E0384-17, www.astm.org.
- [16] D. Seo, K. Ogawa, K. Sakaguchi, N. Miyamoto, and Y. Tsuzuki, "Surface & Coatings Technology Parameter study influencing thermal conductivity of annealed pure copper coatings deposited by selective cold spray processes," *Surf. Coat. Technol.*, vol. 206, no. 8–9, pp. 2316–2324, 2012.

8. Appendix

8.1 Heat Treatment Certifications

PALMDALE HEAT TREATING, INC.
Certification

Order No.: 141761
Date: 04/23/2019
Entry Date: 04/22/2019
Page: 1 of 1

To:
CAL POLY SLO MATERIALS ENGR
1 GRAND AVE
SAN LUIS OBISPO CA 93405

Purchase Order No.:
Packing List No.:
Material: BE CU

HEAT TREATED IN ACCORDANCE WITH CUSTOMER PURCHASE ORDER

Quantity	Part Number / Part Name / Part Description	Pounds
2	GRCOP-42 SAMPLES ID: 2B-17 & 3C-17 (BE CU MTRL) VACUUM ANNEAL @ 1700°F FOR 1 HOUR	


Insp. Type	Scale	Minimum	Maximum	Number	Other
Customer Requirements:					
PROCESS	NONE				NO TEST
Results:					
PROCESS	NONE				

Process Instructions

Step: 1 (TIME & TEMPERATURE PER CUSTOMER P.O.)
VACUUM ANNEAL 1700°F HOLD 1 HR
N2 GAS FAN COOL

Step: 2 CERTIFY PROCESS

Step: 3 DO NOT BLAST
HANDLE PARTS CAREFULLY


 JAMES RODGERS
 QC MANAGER
 PALMDALE HEAT TREATING, INC.

38834 17th STREET EAST PALMDALE CA 93550 Phone: (661) 274-8604 Fax: (661) 274-9007

PALMDALE HEAT TREATING, INC.
Certification

Order No.: 141762
Date: 04/24/2019
Entry Date: 04/22/2019
Page: 1 of 1

To:
CAL POLY SLO MATERIALS ENGR
1 GRAND AVE
SAN LUIS OBISPO CA 93405

Purchase Order No.:
Packing List No.:
Material: BE CU

HEAT TREATED IN ACCORDANCE WITH CUSTOMER PURCHASE ORDER

Quantity	Part Number / Part Name / Part Description	Pounds
2	GRCOP-42 SAMPLES ID: 2B-18 & 3C-18 (BE CU MTRL) VACUUM ANNEAL AT 1800°F FOR 1 HOUR	


Insp. Type	Scale	Minimum	Maximum	Number	Other
Customer Requirements:					
PROCESS	NONE				NO TEST
Results:					
PROCESS	NONE				

Process Instructions

Step: 1 (TIME & TEMPERATURE PER CUSTOMER P.O.)
VACUUM ANNEAL 1800°F HOLD 1 HR
N2 GAS FAN COOL

Step: 2 CERTIFY PROCESS

Step: 3 DO NOT BLAST
HANDLE PARTS CAREFULLY


 JAMES RODGERS
 QC MANAGER
 PALMDALE HEAT TREATING, INC.

38834 17th STREET EAST PALMDALE CA 93550 Phone: (661) 274-8604 Fax: (661) 274-9007